High-Squinted Spaceborne SAR Data Focusing in the Sliding-Spotlight Mode

Yanfang Liu, Wei Yang, *Member, IEEE,* Qi Wei, Hongcheng Zeng, *Member, IEEE,* Wei Liu, *Senior Member, IEEE,* Jie Chen, *Senior Member, IEEE,* Chunsheng Li, Weijie Wang, Weiwei Ji

***Abstract*—Processing high-squinted spaceborne SAR data in the sliding-spotlight mode is a challenging task due to azimuth spectral aliasing and range-azimuth coupling for frequency-domain imaging algorithms, and most critically, the variation of Doppler parameters causes significant reduction in the depth-of- azimuth-focus (DOAF). In this paper, a novel imaging algorithm is proposed for focusing high-squinted spaceborne SAR data in the sliding-spotlight mode. First, linear range walk correction (LRWC) and range frequency-dependent de-rotation are applied to remove the coupling of range frequency with the Doppler parameters. Then, a modified range migration algorithm (RMA) is derived for accurate focusing. The de-ramp operation combined with improved nonlinear chirp scaling (INCS) is employed for solving the aliasing problem of azimuth time and extending the depth-of-azimuth-focus in the third step. Finally, geometry distortion caused by LRWC is corrected. Simulation results are provided to demonstrate the effectiveness of the proposed algorithm.**

***Index Terms*—Synthetic aperture radar (SAR), sliding spot-light, range frequency-dependent de-rotation, the improved non- linear chirp scaling.**

I. Introduction

Spaceborne synthetic aperture radar (SAR) in the sliding- spotlight mode can break through the resolution limitation and achieve lasting illumination of targets by flexible steering of the azimuth antenna [1], [2], which has been widely applied to some high-resolution applications such as target detection and recognitions in recent years [3]. Squinted sliding-spotlight mode SAR provides more flexible patterns than those achievable in traditional sliding-spotlight mode SAR. It has been adopted in current state-of-the-art satellites ICEYE constellation [4][5], Capella constellation [6][7], and Umbra [8] with long imaging dwell times and multi-angle observation. The ICEYE and Capella constellations effectively enhance the imaging quality by the long dwell time and multi-look processing. With the increased illumination time of up to 25 seconds, the squinted angle increases by antenna steering. Umbra has achieved the high squinted spotlight imaging mode with the squinted angle of ± 45 degrees. However, the squinted geometry has made the imaging process more challenging due to two factors: elaborate steering of the azimuth antenna and the squinted observation geometry.

In sliding-spotlight mode SAR, the azimuth bandwidth determined by beam steering of the azimuth antenna should be large enough to achieve high-resolution observation. However, the designed pulse repetition frequency (PRF) is limited to the range ambiguity characteristics of the SAR system. As a result, azimuth spectrum aliasing occurs, and the classical frequency domain imaging algorithms such as RD [9], CS [10], and RMA [11] will fail. To overcome this problem, some methods have been developed. In the spectrum mosaicking method [12], a pretreatment procedure, including spectrum spreading, copying, mosaicking, and filtering, is implemented to recover the unfolding spectrum first. In the sub-aperture method [13][14], the instantaneous azimuth bandwidth follows the Nyquist sampling principle after block processing in the azimuth time domain. However, both methods are inefficient if the azimuth aliasing problem is serious and the azimuth spectrum spans over several PRFs. Therefore, full-aperture methods based on the de-chirp or the de-rotation operation are proposed [15]-[17]. A classical method, named the two-step approach (TSA), resamples the echo data and transforms it into one in the broadside mode by a convolution operation with a reference function. The convolution operation named the de-chirp or the de-rotation operation is achieved by FFT and complex phase multiplication effectively. The reference function is a quadratic phase related to the Doppler frequency modulation rate in TSA. However, the aliasing problem reoccurs in the azimuth time domain. The three-step approach and its improved versions [18]-[21] are proposed for eliminating the effect of azimuth time aliasing by modifying the reference

This work was supported by the National Science Foundation of China (NFSC) under Grant No. 62271028 and No. 62101014, and the Beijing Natural Science Foundation under Grant 4222006. (Corresponding author: HongCheng Zeng).

Yanfang Liu, Wei Yang, Jie Chen, Chunsheng Li, and Hongcheng Zeng are with the School of Electronic and Information Engineering, Beihang University, Beijing 100191, China. (e-mail: by2002162@buaa.edu.cn; yangweigigi@sina.com; chenjie@buaa.edu.cn; chunshengli201@163.com; zenghongcheng@buaa.edu.cn).

Qi Wei is with Beijing Institute of Tracking and Telecommunication Technology, Beijing 100191, China. (e-mail: robyche@163.com).

Wei Liu is with the School of Electronic Engineering and Computer Science, Queen Mary University of London, London E1 4NS, UK (e-mail: w.liu@qmul.ac.uk).

Weijie Wang and Weiwei Ji is with Shanghai Aerospace Electronic Technology Institute, Shanghai 201109, China. (e-mail: buaawwj@163.com; jwwlr@163.com)

function based on the unified-model-coefficient (UMC). However, as the signal bandwidth extends, the extra Doppler bandwidth caused by large bandwidth makes the three-step-based approach inefficient for high-resolution spaceborne SAR processing. The range frequency-dependent de-rotation operation is proposed for solving the azimuth spectrum aliasing induced by the coupling between Doppler frequency modulation rate and high range bandwidth [22]. However, the azimuth interval is also range frequency-dependent after range frequency-dependent de-rotation operation. The azimuth resampling based on the Sinc interpolator is needed to align the sampling grids. In addition, the azimuth spectrum aliasing problem caused by squinted observation is not considered in [22].

Whether in the stripmap mode SAR or the sliding-spotlight mode SAR, the squint observation leads to higher coupling between azimuth and range, and makes accurate focusing more difficult [23]. The coupling is principally represented as significant range walk in the range time domain. Correspondingly, it manifests itself as the high dependence of Doppler parameters on range frequency in the frequency domain. The processing transforms from one-dimensional (1-D) to two-dimensional (2-D) because of presence of significant range walk. Hence, the range and azimuth signal cannot be focused separately. The dependence between Doppler parameters and the range frequency, especially the range frequency-dependent Doppler centroid, makes the 2-D spectrum skew and exacerbates the azimuth spectrum aliasing problem, and therefore it must be carefully considered in the squinted mode SAR. The aim of LRWC is to remove the negative effect of the range frequency-dependent Doppler centroid [21], [24]-[27], but it leads to azimuth variation of the Doppler frequency modulation (FM) rates and reduces the depth of azimuth focus (DOAF). To solve this problem, the azimuth resampling method [26] and the nonlinear chirp scaling-based method [25]-[30] were proposed for equalizing azimuth variation and increasing the DOAF. However, general NCS-based methods do not work when the variable error is significant enough to affect the position of the stationary phase point. Last but not least, the 2-D spatial variation of imaging parameters such as the equivalent velocity and the squint angle becomes more severe in the squint mode and increases the focusing difficulty at the scene edge [31].

In this work, a novel three-step-based (TSB) imaging algorithm with improved nonlinear chirp scaling operation is proposed for improving the focusing performance of the high-squinted spaceborne SAR data in the sliding-spotlight mode. The processing includes azimuth preprocessing, modified RMA, de-ramp operation with the improved NCS algorithm and geometric correction. In azimuth preprocessing, LRWC and the range frequency-dependent de-rotation operation are implemented to remove the coupling of Doppler parameters with range frequency and eliminate azimuth spectrum aliasing caused by signal bandwidth and antenna steering. Then, a modified RMA based on the chirp z-transform (CZT) is derived for focusing. In the third step, the range frequency-dependent de-ramp operation is implemented to equalize the azimuth interval and solve the aliasing problem in azimuth time simultaneously. In addition, an improved NCS algorithm based on the second-order approximations of the stationary phase point is derived and implemented to expand the DOAF. Finally, the position disturbance caused by LRWC is corrected by geometric correction. To summarize, the main contributions of the proposed algorithm are given as follows.

1) Range frequency-dependent de-rotation without azimuth resampling. The azimuth interval is range frequency-dependent after range frequency-dependent de-rotation operation. In the proposed algorithm, the signal is rearranged, and focusing is accomplished without resampling. With the derived range frequency-dependent de-ramp operation to equalize the azimuth interval, the Sinc interpolation is avoided.

2) Modified RMA based on the chirp z-transform. In the proposed algorithm, a modified RMA is derived to focus the azimuth signal while the Stolt interpolation is replaced by the CZT with higher efficiency.

3) Improved NCS algorithm based on the second-order approximations of the stationary phase point. The performance of existing NCS-based algorithms is degraded as the coupling phase caused by the first-order approximations of the stationary phase point increases. In the proposed algorithm, the second-order expression of the stationary phase point is calculated to derive more accurate NCS factors based on series inversion [32][33], and the DOAF is expanded by the improved NCS operation.

The rest of this paper is arranged as follows. Section II introduces the signal model and describes time-frequency properties of the spaceborne squinted sliding-spotlight SAR. The novel imaging algorithm is derived in Section III. Section IV validates the proposed algorithm with simulated SAR data. Finally, conclusions are drawn in Section V.

II. Signal Model and Time-Frequency Properties

In this section, the basic signal model for the spaceborne squinted sliding-spotlight SAR is established, and its time-frequency properties are analyzed to support the derivation of the subsequent algorithm.

A. Signal Model of Squinted Sliding Spotlight SAR

The geometric model of a squinted sliding-spotlight space-borne SAR system is shown in Fig. 1. The SAR sensor travels along the elliptical orbit with range-dependent velocity v_r , transmits and receives a linear frequency modulated pulse periodically. η_a , η_o , and η_b are the start, center, and center of azimuth time. At the same time, azimuth-steering around the rotation point is performed to increase the illumination time of targets. Based on the signal model [18], [19], the received signal for a point target A with the closest range r and center Doppler time t_a can be expressed as

$$S_0(\tau,t;r,t_a)=\sigma\cdot w_r\left[\frac{\tau-2R(t;r,t_a)/c}{T}\right]\cdot w_a\left[\frac{Y(r)t-t_a}{T_{3dB}}\right] \\ \cdot\exp\left\{-j\pi K_r\left(\tau-\frac{2R(t;r,t_a)}{c}\right)^2\right\}\cdot\exp\left\{-j\frac{4\pi R(t;r,t_a)}{\lambda}\right\} \tag{1}$$

where σ is the scattering coefficient, and $w_r[\cdot]$ and $w_a[\cdot]$ are the range and azimuth antenna pattern functions, respectively. They are assumed to have a rectangular envelope $rect[\cdot]$ for convenience in the following sections. τ is the range fast time, t is the azimuth slow time, c is the speed of light, and λ is the wavelength. K_r and T are the chirp rate and pulse width of the transmitted signal, respectively. $Y(r)$ is the hybrid factor, and T_{3dB} is the coherent accumulation time.

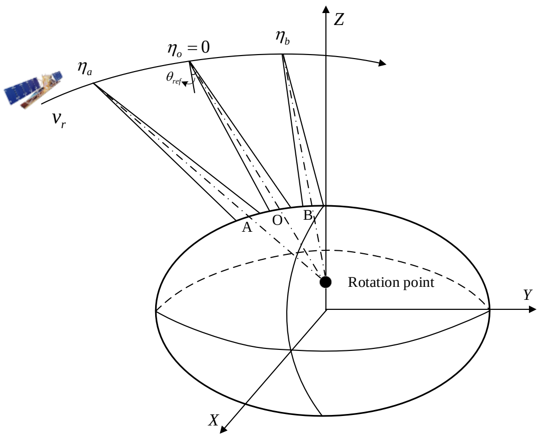

Fig. 1. Geometric model of a squinted sliding-spotlight spaceborne SAR system.

$$Y(r) = \frac{R_{rot} - r}{R_{rot}} \tag{2}$$

$$T_{3dB} = \frac{\lambda \cdot r}{D \cdot v_r \cos\theta_{ref}} \tag{3}$$

where R_{rot} is the closest range between the rotation point and the satellite, D is the length of antenna, and θ_{ref} is the squinted angle of the reference range. $R(t;r_a,t_a)$ is the instantaneous slant range between target A and SAR sensor, and can be modeled by a modified hyperbolic range equation (MHRE) [21].

$$R(t;r,t_a) = \sqrt{r^2 + v_r^2(t-t_a)^2 - 2r \cdot v_r(t-t_a)\sin\theta_{ref}} + \frac{\lambda}{12}\Delta f_3 t^3 \tag{4}$$

where Δf_3 is an invariant third-order coefficient related to orbit and is estimated by numerical approaches. The fourth-order Taylor-series expansion of $R(t;r_a,t_a)$ can be written as

$$R(t;r,t_a) \approx r + \sum_{i=1}^{4} k_i (t-t_a)^i + \frac{\lambda}{12}\Delta f_3 t^3 \tag{5}$$

where $k_i, i = 1,2,3,4$ represent the nth-order coefficient at $t = t_a$. The coefficient k_i is a variable with r, representing spatial variability in range.

B. Time–Frequency Properties in the Range Frequency Domain

Derived from the principle of stationary phase (POSP) [32]-[34], the signal after range Fourier transform (FT) can be expressed as

$$\begin{aligned} S_1(f_\tau,t;r,t_a) &= \sigma \cdot rect\left[\frac{f_\tau}{B_w}\right] \cdot rect\left[\frac{Y(r)t - t_a}{T_{3dB}}\right] \\ &\cdot \exp\left\{-j\pi\frac{f_\tau^2}{K_r}\right\} \cdot \exp\left\{-j\frac{4\pi}{c}(f_\tau + f_c)R(t;r,t_a)\right\} \end{aligned} \tag{6}$$

where f_τ and f_c are the range frequency and the center frequency, respectively, B_w is the signal bandwidth. The first exponential term is the frequency modulation (FM) of range signal. The second exponential term represents the range-azimuth coupling term. Ignoring the effect of curved orbit, the coupling phase term has the following form:

$$\phi_1(f_\tau,t;r,t_a) = -\frac{4\pi}{c}(f_\tau + f_c) \cdot \left(r + \sum_{i=1}^{4} k_i(r) \cdot (t-t_a)^i\right) \tag{7}$$

The Doppler centroid and Doppler rate range [35] can be calculated by

$$\begin{aligned} f_d(f_\tau,t;r,t_a) &= \frac{1}{2\pi} \cdot \frac{\partial \phi_1(f_\tau,t;r,t_a)}{\partial t} \\ &= -\frac{2}{c}(f_\tau + f_c) \cdot \left(\sum_{i=1}^{4} i \cdot k_i(r) \cdot (t-t_a)^{i-1}\right) \end{aligned} \tag{8}$$

$$\begin{aligned} f_r(f_\tau,t;r,t_a) &= \frac{1}{2} \cdot \frac{\partial f_d(f_\tau,t;r,t_a)}{\partial t} \\ &= -\frac{2}{c}(f_\tau + f_c) \cdot \left(\sum_{i=2}^{4} i \cdot (i-1) \cdot k_i(r) \cdot (t-t_a)^{i-2}\right) \end{aligned} \tag{9}$$

Taking points located at the reference range r_{ref} as an example, the Doppler centroid and Doppler rate become

$$f_{d0}(f_\tau) = -\frac{2}{c}(f_\tau + f_c) \cdot k_1(r_{ref}) \tag{10}$$

$$f_{r0}(f_\tau) = -\frac{2}{c}(f_\tau + f_c) \cdot k_2(r_{ref}) \tag{11}$$

$$k_1(r_{ref}) = -v_{ref}\sin\theta_{ref} \tag{12}$$

$$k_2(r_{ref}) = \frac{v_{ref}^2 \cos^2\theta_{ref}}{2r} \tag{13}$$

As shown in (10) and (11), both Doppler parameters are related to range frequency f_τ. The invariant term of Doppler parameters is analyzed at first. Time–frequency diagram (TFD) of targets located at near, center, and far azimuth lines with center frequency f_c is shown in Fig. 2(a). The Doppler bandwidth $B_w(f_c)$ contains two parts:

$$B_w(f_c) = B_{3dB} + B_{steer}(f_c) = B_{3dB} + k_\theta(f_c) \cdot T \tag{14}$$

$$k_\theta(f_\tau) = \frac{2v_r^2}{cR_{rot}} f_\tau,\ f_\tau \in [-f_s/2 + f_c, f_c + f_s/2] \tag{15}$$

where B_{3dB} is the Doppler bandwidth corresponding to the 3dB beam width of the azimuth antenna, $B_{steer}(f_c)$ is achieved by the steering of azimuth antenna, $k_\theta(f_c)$ is the steering rate, and $T = T_a + t_{far} - t_{near}$ is the observation time of radar. T_a is the coherent accumulation time of targets. t_{far}, t_{center}, and t_{near} are the azimuth time of the target located at near, center, and far azimuth lines respectively. It can be concluded that the Doppler bandwidth $B_w(f_c)$ spans over several PRFs and azimuth spectrum aliasing arises inevitably. Therefore, the problem of azimuth spectrum aliasing needs to be solved first for a frequency domain imaging algorithm.

Considering the impact of range frequency f_τ, TFDs of targets with range frequency $f_c - f_s/2$, f_c, and $f_c + f_s/2$ are shown in Fig. 2(b), where the total Doppler bandwidth B_{total} is

$$\begin{aligned} B_{total} &= B_w(\Delta f_d) + B_{3dB} + \left(k_\theta(f_c - f_s/2) + k_\theta(f_c + f_s/2)\right)\cdot\frac{T}{2} \\ &= B_w(\Delta f_d) + B_{3dB} + B_{steer}(f_c) \end{aligned} \tag{16}$$

The dependence between the Doppler centroid f_d and range frequency induces the extra bandwidth $B_w(\Delta f_d)$ and makes azimuth spectrum aliasing worse. The dependence between the steering rate and range frequency makes aliasing incomplete. They must be considered in the squinted sliding-spotlight spaceborne SAR.

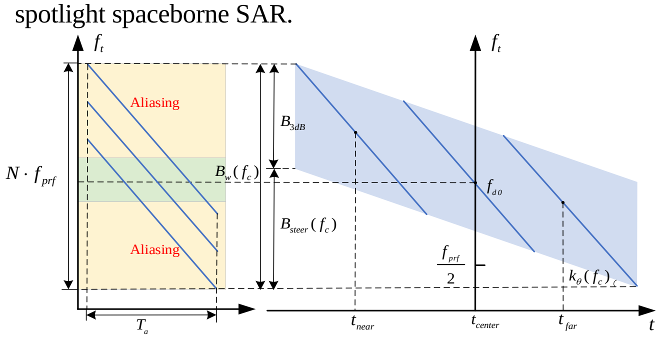

(a) TFDs of targets located at near, center, and far azimuth lines with center frequency.

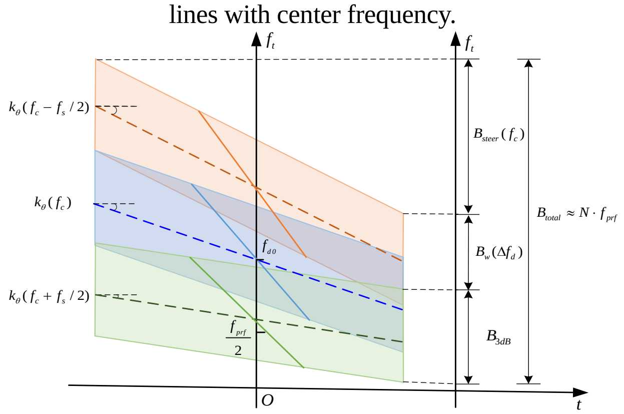

(b) TFDs of targets with range frequency $f_c - f_s/2$, f_c, and $f_c + f_s/2$.

Fig. 2. Time–frequency analysis.

III. Algorithm Description

Based on the time–frequency analysis in Section II, an improved algorithm based on the three-step approach [18] is introduced in this part. The flowchart of the proposed algorithm is shown in Fig. 3, including four main steps. The key steps are marked in yellow.

Step 1: Range compression and azimuth preprocessing. Range matched filtering and azimuth spectrum reconstruction without aliasing is completed in the range frequency domain. Because of the range frequency-dependent de-rotation operation, the azimuth interval is also range frequency-dependent after azimuth spectrum reconstruction. The signal is rearranged and focusing is accomplished first without the azimuth resampling of the sampling grids. A range frequency-dependent de-ramp operation is derived to equalize the azimuth interval in Step 3.

Step 2: Focusing by a modified RMA. After signal model adjustment, a modified RMA is derived to focus the azimuth signal in the range frequency domain, in which the time-consuming Stolt interpolation is replaced by the chirp-Z transform, and the efficiency is improved.

Step 3: Azimuth processing by improved NCS algorithm. Precise focusing of azimuth signal and azimuth time de-aliasing is achieved by an improved NCS algorithm based on the second-order expression of the stationary phase point.

Step 4: Geometric correction. The deviation of the range focusing position induced by LRWC is corrected in this part.

A. Range Compression and Azimuth Preprocessing

Range compression and curved orbit correction are carried out by phase multiplication at first. Then, the 2-D unfolded signal is recovered by LRWC and range frequency-dependent de-rotation, where LRWC is used to remove the linear component of range cell migration (RCM), and range frequency-dependent de-rotation is applied to relax the second-order range-azimuth coupling. The details are given as follows.

After range FT, the signal is given in (6). Range compression and curved orbit correction should be completed simultaneously by phase multiplication with filter $H_1(f_\tau, t; r, t_a)$.

$$H_2(f_\tau, t) = \exp\left\{ j\frac{4\pi}{c}(f_\tau + f_c)\cdot k_1(\theta_{ref})\cdot t \right\} \tag{17}$$

As analysed in Section II-B, the dependence of Doppler parameters on range frequency is the dominant component of azimuth spectrum aliasing in the squinted sliding-spotlight spaceborne SAR. LRWC operation, as given in (18), is performed to remove the Doppler ambiguity because Doppler centroid is outside the PRF.

$$H_2(f_\tau, t) = \exp\left\{ j\frac{4\pi}{c}(f_\tau + f_c)\cdot k_1(\theta_{ref})\cdot t \right\} \tag{18}$$

There exists a noticeable shift related to t_a along range lines after LRWC processing. The severe mismatch of Doppler parameter posed by the shift will lead to defocusing in classic imaging algorithms. The azimuth signal is processed efficiently by changing the focused domain to range frequency domain in this paper. More importantly, the negative effect of LRWC is fully circumvented. After range compression, curved orbit correction and LRWC, the signal is represented as $S_2(f_\tau, t; r, t_a)$.

Besides, the de-rotation technique, which has been verified effectively in [15]-[22], implements a convolution

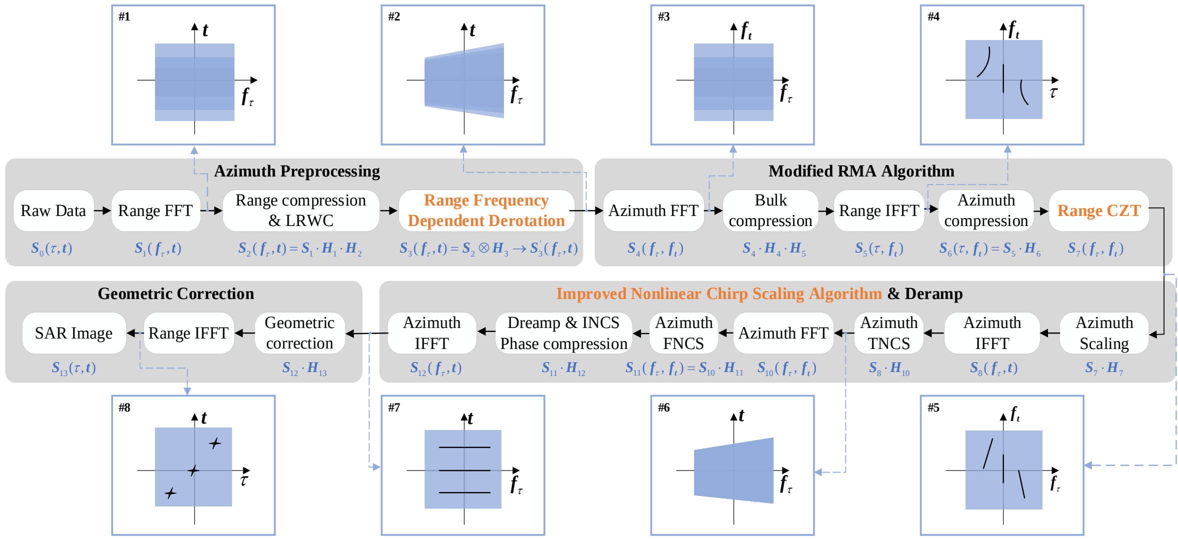

Fig.3. Flowchart of the proposed algorithm.

with a quadratic phase function to remove azimuth spectrum aliasing caused by antenna beam rotation. Its performance is evaluated by TFDs with respect to different range frequency bins as shown in Fig. 4(a). In Fig. 4, the TFD of targets with range frequency bin in $f_c - f_s/2$, f_c, and $f_c + f_s/2$ is represented by green, red, and yellow colours, respectively, and the blue block embodies the time-frequency width of the azimuth signal. As shown in Fig. 4(a), only the TFD with the center frequency f_c is fully corrected while others still have a slope. It indicates that azimuth spectrum aliasing will emerge with high probability with increase of the transmission signal bandwidth.

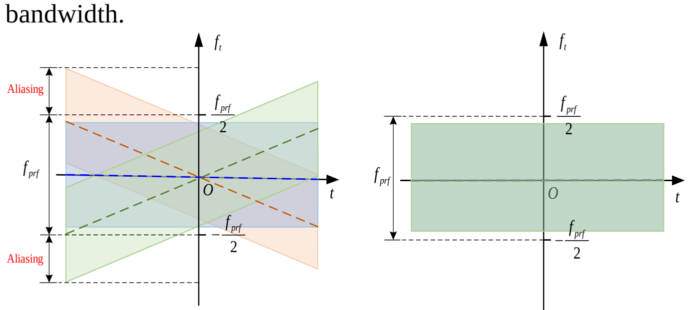

(a) (b)

Fig.4. TFDs of targets with range frequency $f_c - f_s/2$, f_c, and $f_c + f_s/2$ after de-rotation: (a) de-rotation in range time doma in; (b) range frequency-dependent de-rotation.

In this paper, the range frequency-dependent de-rotation is applied to eliminate the aliasing effect caused by signal bandwidth as shown in Fig. 4(b). The range frequency-dependent de-rotation is given by

$$S_3(f_\tau,t;r,t_a) = S_2(f_\tau,t;r,t_a) \otimes H_3(f_\tau,t;r,t_a) \tag{19}$$

$$H_3(f_\tau,t) = \exp\left\{ j\pi \frac{f_\tau + f_c}{f_c} \cdot k_w t^2 \right\} \tag{20}$$

where $\otimes$ represents convolution and

$$k_w = \frac{2v_{ref}^2 \cos^2\theta_{ref}}{\lambda R_{rot}} \tag{21}$$

Expand (19) as

$$\begin{aligned} S_3(f_\tau,t;r,t_a) &= \exp\left\{ j\pi \frac{f_\tau + f_c}{f_c} \cdot k_w t^2 \right\} \\ &\cdot \int_{-\infty}^{\infty} \xi(f_\tau,u;r,t_a) \cdot \exp\left\{ -j\pi \frac{f_\tau + f_c}{f_c} \cdot 2k_w t \cdot u \right\} du \end{aligned} \tag{22}$$

where

$$\xi(f_\tau,u;r,t_a) = S_2(f_\tau,u;r,t_a) \cdot \exp\left\{ j\pi \frac{f_\tau + f_c}{f_c} \cdot k_w u^2 \right\} \tag{23}$$

As shown in (22) and (23), the convolution operation is realized quickly by two quadratic phase multiplications and an azimuth FT. After azimuth FT, the azimuth frequency is extended sufficiently, and the new equivalent PRF is

$$f_{prf} = \frac{N_a \cdot k_w}{PRF} \cdot \frac{f_\tau + f_c}{f_c} \tag{24}$$

where N_a is the number of azimuth samples. The discrete azimuth time is

$$t = j \cdot \frac{1}{f_{prf}} = j \cdot \frac{PRF}{N_a \cdot k_w} \cdot \frac{f_c}{f_\tau + f_c}, \; j = 1,2,\cdots,M \tag{25}$$

As shown above, the discrete azimuth time is range frequency dependent. Classical methods cannot be directly applied, and it is necessary to improve the focusing algorithm in the next section.

Accordingly, the signal after LRWC and range frequency -dependent de-rotation becomes

$$\begin{aligned} S_3(f_\tau,t;r,t_a) &\approx rect\left[\frac{f_\tau}{B_w}\right] \cdot rect\left[-\frac{t}{T_s}\right] \\ &\cdot \exp\left\{ j\frac{4\pi}{c}(f_\tau + f_c)\cdot k_1(r)\cdot t_a \right\} \\ &\cdot \exp\left\{ -j\frac{4\pi}{c}(f_\tau + f_c)\cdot \begin{pmatrix} r - k_e(r)\cdot(t-t_a)^2 \\ +\sum_{i=3}^{4} k_i(r)\cdot(t-t_a)^i \end{pmatrix} \right\} \end{aligned} \tag{26}$$

$$k_e(r) = \frac{2v_r^2 \cos^2\theta}{\lambda(R_{rot} - r)} \tag{27}$$

B. Focusing with Modified RMA

After LRWC and range frequency-dependent de-rotation, the Doppler frequency spreads while the time width narrows. The signal $S_3(f_\tau, t; r, t_a)$ is equivalent to a stripmap SAR data overlapped at azimuth center time $t = 0$. However, existing stripmap SAR imaging algorithms cannot be directly applied because the sampling interval in azimuth is related to the range frequency bin as shown in (25). It is necessary to modify the model of $S_3(f_\tau, t; r, t_a)$ with consideration for nonuniform sampling. With $t = \frac{f_c}{f_\tau + f_c} t^{'}$, $S_3(f_\tau, t; r, t_a)$ is rewrote as

$$\begin{aligned} S_3^{'}\left(f_\tau, t^{'}; r, t_a\right) &= rect\left[\frac{f_\tau}{B_w}\right] \cdot rect\left[-\frac{\frac{f_c}{f_\tau + f_c} t^{'}}{T_s}\right] \\ &\cdot \exp\left\{ j\frac{4\pi}{c}(f_\tau + f_c) \cdot k_1(r) \cdot t_a \right\} \\ &\cdot \exp\left\{ -j\frac{4\pi}{c}(f_\tau + f_c) \left(\begin{array}{l} r - k_e(r) \cdot (\frac{f_c}{f_\tau + f_c} t^{'} - t_a)^2 \\ + \sum_{i=3}^{4} k_i(r) \cdot (\frac{f_c}{f_\tau + f_c} t^{'} - t_a)^i \end{array} \right) \right\} \end{aligned} \tag{28}$$

where

$$t^{'} = i \cdot \frac{PRF}{N_a \cdot k_w} \tag{29}$$

As shown in (28), $S_3^{'}(f_\tau, t^{'}; r, t_a)$ is equivalent to the stripmap SAR signal after Keystone transform [35], and the linear coupling term is eliminated. But the Doppler frequency modulation rate is turned into $-k_e(r)$ from $k_r(r)$, where $k_r(r) = 2v_r^2 \cos^2\theta / \lambda / r$. The Doppler FM rate is compensated firstly in the azimuth frequency domain with the quadratic phase

$$H_4(f_\tau, f_t) = \exp\left(j\pi \cdot \frac{f_\tau + f_c}{f_c} \cdot \frac{f_t^2}{k_w} \right) \tag{30}$$

Data focusing is accomplished conveniently by an adjustment of the stripmap SAR imaging algorithms based on detailed analysis of the signal $S_3^{'}(f_\tau, t^{'}; r, t_a)$. In this section, a modified RMA is proposed.

First, the signal is transformed into the 2-D spectrum domain by applying the principle of stationary phase. The stationary phase point t_k and the signal is expressed as in (31) and (32).

$$\frac{f_c}{f_\tau + f_c} t_k - t_a = \frac{r}{v_r} \cdot \left(\cos(\theta) - \sin(\theta) \frac{D_f(f_t)}{\sqrt{1 - \left(D_f(f_t) \cdot \frac{v_{ref}}{v_r} \right)^2}} \right) \tag{31}$$

$$\begin{aligned} S_4(f_\tau, f_t; r, t_a) &\approx rect\left[\frac{f_\tau}{B_w}\right] \cdot rect\left[-\frac{f_t / k_e + t_a}{T_s}\right] \\ &\cdot \exp\left\{ -j\frac{4\pi}{c}(f_\tau + f_c) \cdot r \cdot H_f\left(f_t, v_r, \theta\right) \right\} \\ &\cdot \exp\left\{ -j\frac{4\pi}{c}(f_\tau + f_c) \cdot v_{ref} \cdot D_f(f_t) \cdot t_a \right\} \end{aligned} \tag{32}$$

where

$$D_f(f_t) = \cos(\theta_{ref}) + \frac{\lambda f_t}{2v_{ref}} \tag{33}$$

$$\begin{aligned} H_f\left(f_t, v_r, \theta\right) &= \sin(\theta) \cdot \sqrt{1 - \left(D_f(f_t) \cdot \frac{v_{ref}}{v_r} \right)^2} \\ &+ \cos(\theta) \cdot D_f(f_t) \cdot \frac{v_{ref}}{v_r} \end{aligned} \tag{34}$$

In (32), on the one hand, the azimuth envelope of $S_4(f_\tau, f_t; r, t_a)$ is independent of range frequency, while on the other hand, for the azimuth phase there exists coupling only between azimuth frequency f_t and the linear term of range frequency $f_\tau + f_c$. The RCMC is completed after the range scaling of $f_\tau + f_c$.

$$(f_\tau + f_c) \cdot r \cdot H_f\left(f_t, v_r, \theta\right) \Rightarrow (f_\tau^{'} + f_c^{'}) \cdot r \tag{35}$$

where $f_\tau^{'} = f_\tau \cdot H_f\left(f_t, v_r, \theta\right)$, and $f_c^{'} = f_c \cdot H_f\left(f_t, v_r, \theta\right)$. After range scaling, the coupling between $f_\tau^{'} + f_c^{'}$ and f_t is eliminated.

In addition, the spatial-variant properties of $H_f\left(f_t, v_r, \theta\right)$ along the range direction must be considered. In practice, the equivalent velocity v_r and squinted angle θ follow a steady change with range r, which must be taken into account. Then a Taylor expansion of $r \cdot H_f\left(f_t, v_r, \theta\right)$ with Δr is performed (see Appendix). Expanding this as

$$\begin{aligned} \phi_4(f_\tau, f_t; r, t_a) &= \frac{4\pi}{c}(f_\tau + f_c) \\ &\cdot \left\{ r_{ref} \cdot H_{f0}(f_t) + H_f^{'}(f_t) \cdot \Delta r + \Delta H_f \cdot O(\Delta r^2) \right\} \end{aligned} \tag{36}$$

where

$$H_{f0}\left(f_t\right) = \sin(\theta_{ref}) \cdot \sqrt{1 - D_f^2(f_t)} + \cos(\theta_{ref}) \cdot D_f(f_t) \tag{37}$$

$$H_f^{'}(f_t) = H_{f0}(f_t) + r_{ref} \cdot k_{v_r}^{'} + r_{ref} \cdot k_\theta^{'} \tag{38}$$

As shown in (36), the phase term is composed of three parts. The first is the reference phase of the scene center, which is compensated to achieve azimuth coarse focusing. The second term denotes the range scaling phase, which represents the residual RCM and the residual range-azimuth coupling. To perform accurate focusing, range scaling operation and phase compensation are implemented, providing a decoupled result between azimuth modulation $H_f\left(f_t, v_r, \theta\right)$ and range frequency $f_\tau + f_c$. The third term is the higher-order phase error, which induces a negative effect on azimuth edge of the scene. To illustrate the influence of the higher-order term, the phase error curve using the parameters listed in Table I is presented in Fig. 5, where it can be seen that the maximum phase error due to this term is less than $\pi/4$. Therefore, the higher-order term is ignored in this paper.

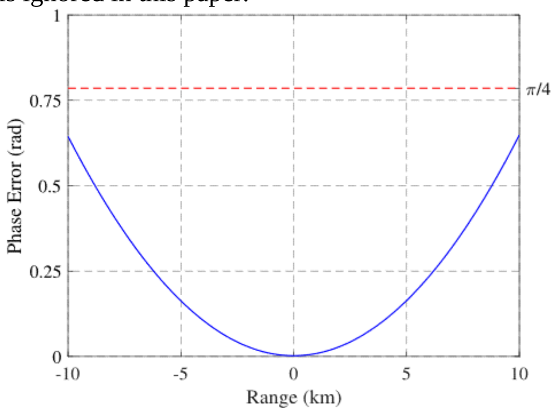

Fig. 5. The phase error caused by the third term of ϕ_4.

The following discussion will focus on the detailed processing procedure. First, bulk focusing is completed by multiplying the reference function,

$$H_5(f_\tau, f_t) = \exp\left(j\frac{4\pi}{c}(f_\tau + f_c)\cdot r_{ref}\cdot H_{f0}(f_t) \right) \tag{39}$$

After bulk focusing and range IFT, the signal becomes

$$\begin{aligned} S_5(\tau, f_t; r, t_a) &= \mathrm{Sinc}\left[\tau - \frac{2\Delta r\cdot H_f^{'}(f_t)}{c} - \frac{2v_r\cdot D_f(f_t)\cdot t_a}{c} \right] \\ &\cdot rect\left[-\frac{f_t/k_e + t_a}{T_s} \right]\cdot \exp\left\{ -j\frac{4\pi}{c} f_c\cdot \begin{pmatrix} \Delta r\cdot H_f^{'}(f_t) + \\ v_r\cdot D_f(f_t)\cdot t_a \end{pmatrix} \right\} \end{aligned} \tag{40}$$

Focusing is performed by the range scaling transformation and the phase multiplication. In the range time domain, the target is focused at

$$\tau = \frac{2\cdot\Delta r\cdot H_f^{'}(f_t)}{c} + \frac{2v_r\cdot D_f(f_t)\cdot t_a}{c} \tag{41}$$

To eliminate the coupling phase between $H_f^{'}(f_t)$ and f_c, we construct the azimuth compensation function as follows:

$$H_6(\tau, f_t) = \exp\left(j2\pi\cdot f_c\cdot\tau\cdot\left(1 - \frac{1}{H_f^{'}(f_t)} \right) \right) \tag{42}$$

With azimuth compensation operation, $S_5(\tau, f_t; r, t_a)$ can be rearranged as

$$\begin{aligned} S_6(\tau, f_t; r, t_a) &= \mathrm{Sinc}\left[\tau - \frac{2\Delta r\cdot H_f^{'}(f_t)}{c} - \frac{2v_r\cdot D_f(f_t)\cdot t_a}{c} \right] \\ &\cdot rect\left[-\frac{f_t/k_e + t_a}{T_s} \right]\cdot \exp\left\{ -j\frac{4\pi}{c} f_c\cdot\Delta r \right\} \\ &\cdot \exp\left\{ -j\frac{4\pi}{c} f_c\cdot v_r\cdot\frac{D_f(f_t)}{H_f^{'}(f_t)}\cdot t_a \right\} \end{aligned} \tag{43}$$

Then the range scaling operation is performed based on range CZT to mitigate the coupling effects between $H_f^{'}(f_t)$ and f_τ. The range frequency axis is rescaled as

$$f_\tau = f_\tau\cdot H_f^{'}(f_t) \tag{44}$$

The discrete range CZT [20], [36] is implemented by FFT and phase multiplications as follows:

$$\begin{aligned} CZT[s(k)] &= W^{\frac{k^2}{2}}\cdot\sum_{i=0}^{M-1}\left(s(i)A^{-i}W^{\frac{i^2}{2}} \right)\cdot W^{\frac{(i-k)^2}{2}} \\ &= W^{\frac{k^2}{2}}\cdot \mathrm{IFFT}\left[\mathrm{FFT}\left(s(m)A^{-m}W^{\frac{m^2}{2}} \right)\cdot \mathrm{FFT}\left(W^{\frac{m^2}{2}} \right) \right] \end{aligned} \tag{45}$$

$$W = \exp\left(-j\pi\frac{2\gamma}{N} \right) \tag{46}$$

$$A = \exp(-j\pi\gamma) \tag{47}$$

where N is the number of FFT points, γ is the scaling factor. In the proposed algorithm, γ is equal to $H_f^{'}(f_t)$.

The azimuth compensation operation and the range scaling operation correspond to the Stolt interpolation in the RMA. After Stolt interpolation, the signal in the range frequency domain is represented as

$$\begin{aligned} S_7(f_\tau, f_t; r, t_a) &\approx rect\left[\frac{f_\tau}{B_w} \right] rect\left[-\frac{f_t/k_e + t_a}{T_s} \right] \\ &\cdot \exp\left\{ -j\frac{4\pi}{c}(f_\tau + f_c)\cdot\left(r + v_{ref}\cdot\frac{D_f(f_t)}{H_f^{'}(f_t)}\cdot t_a \right) \right\} \end{aligned} \tag{48}$$

The phase related to azimuth focusing is

$$\phi_7(f_\tau, f_t; r, t_a) = \frac{4\pi}{c}(f_\tau + f_c)\cdot v_{ref}\cdot\frac{D_f(f_t)}{H_f^{'}(f_t)}\cdot t_a \tag{49}$$

Expanding the phase term ϕ_7 into a Taylor series of f_t yields

$$\begin{aligned} \phi_7(f_\tau, f_t; r, t_a) &\approx -\frac{4\pi}{c}(f_\tau + f_c)\cdot v_{ref}\cdot\cos(\theta_c)\cdot t_a \\ &-2\pi\cdot\frac{f_\tau + f_c}{f_c}\cdot f_t\cdot t_a - \pi\frac{f_\tau + f_c}{f_c}\cdot t_a\cdot\left(l_2\cdot f_t^2 + l_3\cdot f_t^3 \right) \end{aligned} \tag{50}$$

Symmetrical to the range frequency-dependent de-rotation operation, the range frequency-dependent de-ramp operation is performed to avoid azimuth aliasing in the time domain, which is given by

$$H_7(f_\tau, f_t) = \exp\left(-j\pi\cdot\frac{f_\tau + f_c}{f_c}\cdot\frac{f_t^2}{k_e} \right) \tag{51}$$

After range frequency-dependent de-ramp operation, the signal $S_8(f_\tau, t; r, t_a)$ in the azimuth time domain is obtained by azimuth inverse Fourier transform (IFT).

$$\begin{aligned} S_8(f_\tau, t; r, t_a) &\approx rect\left(\frac{f_\tau}{B_w} \right) rect\left(-\frac{\frac{f_c}{f_\tau + f_c}t}{\frac{\lambda R_{rot}}{Dv_e}} \right) \\ &\cdot \exp\left(-\frac{4\pi}{c}(f_\tau + f_c)\cdot v_{ref}\cdot\cos(\theta_c)\cdot t_a \right)\cdot \\ &\cdot \exp\left(j\pi\cdot\frac{f_\tau + f_c}{f_c}\cdot k_e\left(\frac{f_c}{f_\tau + f_c}t - t_a \right)^2 \right)\cdot \\ &\cdot \exp\left(-j\pi\frac{f_\tau + f_c}{f_c}\cdot t_a\cdot\begin{pmatrix} l_2\cdot k_e^2\cdot\left(\frac{f_c}{f_\tau + f_c}t - t_a \right)^2 \\ + l_3\cdot k_e^3\cdot\left(\frac{f_c}{f_\tau + f_c}t - t_a \right)^3 \end{pmatrix} \right) \end{aligned} \tag{52}$$

where v_e is the ground velocity of the beam footprints. The residual phase is given by

$$\begin{aligned}\phi_8(f_\tau,t;r,t_a) = & \underbrace{-\frac{4\pi}{c}(f_\tau+f_c)\cdot v_{ref}\cdot\cos(\theta_c)\cdot t_a + 2k_e t_a\cdot t}_{(1)} \\ & \underbrace{+\frac{f_\tau+f_c}{f_c}\cdot\left(k_e\cdot\left(\frac{f_c}{f_\tau+f_c}t\right)^2\right)}_{(2)} \\ & \underbrace{+\frac{f_\tau+f_c}{f_c}\cdot\left(\begin{array}{l} A(t_a)+B(t_a)\cdot\left(\frac{f_c}{f_\tau+f_c}t\right)+ \\ C(t_a)\cdot\left(\frac{f_c}{f_\tau+f_c}t\right)^2+D(t_a)\cdot\left(\frac{f_c}{f_\tau+f_c}t\right)^3\end{array}\right)}_{(3)}\end{aligned} \tag{53}$$

According to (53), the residual phase can be divided into three parts. The first one is related to the position of the target in range and azimuth and has no effect on focusing. The second one can be completely removed by phase multiplication. The third is the residual phase varying with the azimuth position t_a, which is equalized by an azimuth nonlinear chirp scaling operation in the next section.

C. Azimuth processing by Improved NCS Algorithm

The efficiency of the NCS algorithm is achieved in that the perturbation phase is too small to affect the solution of the stationary phase point. However, a higher residual phase indicates a higher perturbation phase and induces a significant calculation error of the stationary phase point. In order to analyze the effect of the perturbation phase, taking the third-order perturbation function as an example, we derive the performance limitation of the NCS algorithm. The required perturbation function is

$$H_8(f_\tau,f_t)=\exp\left(-j\pi\frac{f_c+f_\tau}{f_c}\cdot b_3\cdot f_t^3\right) \tag{54}$$

The third-order perturbation phase equalizes the azimuth LFM in (50) varying with the azimuth time t_a. Suppose H_8 is invalid to the solution of POSP based on the traditional NCS algorithm [28][29]. Adding (50) with the phase of (54), we have

$$b_3=\frac{l_2}{3k_e} \tag{55}$$

The second-order expression of the stationary phase point f_{tk} is deduced by series reversion considering the negative effect of the perturbation phase, which is given by

$$f_{tk}=A_1\cdot(t-t_a)+A_2\cdot(t-t_a)^2 \tag{56}$$

$$A_1=\frac{1}{1/k_e+l_2t_a} \tag{57}$$

$$A_2=-\frac{b_3}{(1/k_e+l_2t_a)^3} \tag{58}$$

Then, we obtain the phase error induced by the linear approximation of the stationary phase point as

$$\Delta\phi_9(f_\tau,t;r,t_a)= \pi\frac{f_\tau+f_c}{f_c}\cdot\frac{9}{4}\cdot\left\{\begin{array}{l}-A_1^2A_2\left(b_3+2l_3t_a\right)\cdot(t-t_a)^4+ \\ A_1A_2^2\left[3b_3\cdot\left(b_3+l_3t_a\right)\right]\cdot(t-t_a)^5+ \\ -A_2^3\left[1.5\cdot\left(b_3+l_3t_a\right)\right]\cdot(t-t_a)^6\end{array}\right\} \tag{59}$$

$$t-t_a\in\left[-\frac{f_{prf}}{2k_w},\frac{f_{prf}}{2k_w}\right],t_a\in\left[-\frac{X_s}{2v_e},\frac{X_s}{2v_e}\right] \tag{60}$$

The phase error $\Delta\phi_9$ in (59) should be kept under $\pi/4$. According to (59)-(60), the valid range of the azimuth is determined as

$$X_s<\frac{v_e}{2l_3}\left\{\frac{2k_a^5}{b_3}\cdot\frac{\frac{1}{36}\cdot\frac{f_c}{f_s/2+f_c}\cdot\left(\frac{2k_w}{f_{prf}}\right)^4-\frac{b_3^2}{4k_a^5}}{\left\{-1+\frac{3b_3f_{prf}}{4k_a^2k_w}+\frac{3b_3^2f_{prf}^2}{16k_a^3k_w^2}\right\}}-b_3\right\} \tag{61}$$

Simulations using the parameters in Table I are carried out. As shown in Fig. 6, the phase error exceeds the threshold value $\pm\pi/4$ at about ±500 m, which makes the traditional NCS algorithm only valid in small regions.

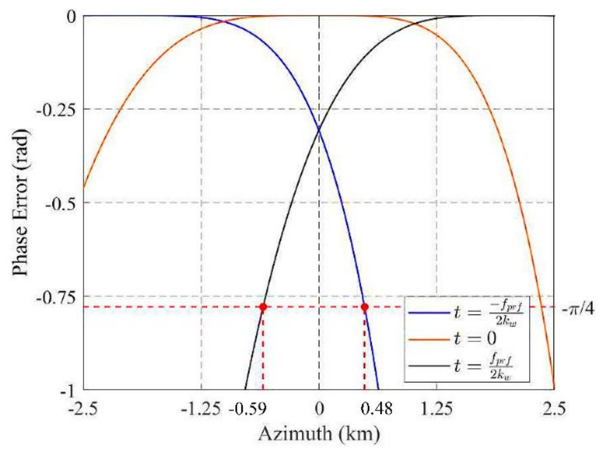

Fig. 6. The phase error induced by first-order approximation of the stationary phase point.

Furthermore, the fourth-order perturbation phase is applied to remove the third-order azimuth-variant phase in (54). However, a second order phase related to t_a^2 is generated at the same time and affects the final results. To solve the problem, the fifth-order prefiltering function is applied first in the azimuth time domain, which is given by

$$H_{10}(f_\tau,t)=\exp\left(-j\pi\frac{f_c+f_\tau}{f_c}\cdot a_4\cdot t^4\right) \tag{62}$$

Multiplying (52) by (62) and transforming the signal into the azimuth frequency domain using POSP yields

$$\begin{aligned}&\phi_{10}(f_\tau,f_t;r,t_a)=\\&-\frac{4\pi}{c}(f_\tau+f_c)\cdot v_{ref}\cdot\cos(\theta_c)\cdot t_a-2\pi\cdot\frac{f_\tau+f_c}{f_c}\cdot f_t\cdot t_a\\&-\pi\frac{f_\tau+f_c}{f_c}\frac{f_t^2}{k_e}-\pi\frac{f_\tau+f_c}{f_c}\cdot t_a\cdot\left(l_2\cdot f_t^2+l_3\cdot f_t^3\right)\\&-\pi\frac{f_\tau+f_c}{f_c}\cdot t_a\cdot\left(a_3\cdot\left(t_a+\left(1/k_e+l_2t_a\right)\cdot f_t\right)^3\right)\end{aligned}\tag{63}$$

The fourth-order NCS phase is introduced to equalize the azimuth-variant quadratic coefficient and cubic coefficient of the Doppler parameters.

$$\begin{aligned}&H_{11}(f_\tau,f_t)=\\&\exp\left(-j\pi\frac{f_c+f_\tau}{f_c}\cdot\left(b_2\cdot f_t^2+b_3\cdot f_t^3+b_4\cdot f_t^4\right)\right)\end{aligned}\tag{64}$$

Based on the second-order expression in (56), the phase of azimuth signal is transformed into the time domain by azimuth IFFT, which is given by

$$\begin{aligned}\phi_{11}(f_\tau,f_t;r,t_a)\approx{}&A(t^2,t^3,t^4,t^5,a_4,b_2,b_3,b_4)\\&+B(b_2)t\cdot t_a+C(b_2,b_3)t^2\cdot t_a\\&+D(a_4,b_2,b_3,b_4)t^3\cdot t_a\\&+E(a_4,b_2,b_3,b_4)t^2\cdot t_a^2\\&+F(a_4,b_2,b_3,b_4,t_a,t_a^2,t_a^3)\end{aligned}\tag{65}$$

To eliminate the azimuth-variant phase related to azimuth compression, the first-order coupling term $B(b_2)$ is set to $2\cdot\alpha\cdot k_e$, and the other terms are set to zero. Let

$$\begin{cases}B(b_2)=2\cdot\alpha\cdot k_e\\C(b_2,b_3)=0\\D(a_4,b_2,b_3,b_4)=0\\E(a_4,b_2,b_3,b_4)=0\end{cases}\tag{66}$$

Then, we obtain the solution to the NCS factors, given by

$$\begin{cases}a_4=\dfrac{-9k_e^2l_2b_2b_3+3l_3k_e^2b_2^2+27k_e^2b_3^2+2k_el_2^2b_2}{l_2k_e\cdot(k_eb_2+1)}\\\qquad+\dfrac{-18k_el_2b_3+9l_3k_eb_2+2l_2^2+6l_3}{l_2k_e\cdot(k_eb_2+1)}\\b_2=-\dfrac{\alpha-1}{\alpha k_e}\\b_3=\dfrac{l_2\cdot\left(b_2+1/k_e\right)}{3}\\b_4=\dfrac{2b_2k_e^3l_2^2-9b_3k_e^3l_2+3l_3b_2k_e^3+2k_e^2l_2^2+3l_3k_e^2}{l_2\cdot(k_eb_2^2+b_2)}\end{cases}\tag{67}$$

In (66), α is set to be around 1 to ensure accuracy of the focusing position. After the INCS operation, we can compensate the residual phase by

$$\begin{aligned}&H_{12}(f_\tau,t)=\\&\exp\left(-j\pi\frac{f_c+f_\tau}{f_c}\cdot A(t^2,t^3,t^4,t^5,a_4,b_2,b_3,b_4)\right)\end{aligned}\tag{68}$$

Here only the first-order coupling term related to the real position of the targets is retained. After azimuth IFT, the 2D focused image is obtained, which is given by

$$\begin{aligned}S_{12}(f_\tau,t;r,t_a)\approx{}&rect\left(\frac{f_\tau}{B_w}\right)\sin c\left(t-k_et_a\right)\\&\cdot\exp\left(-\frac{4\pi}{c}(f_\tau+f_c)\cdot v_{ref}\cdot\cos(\theta_c)\cdot t_a\right)\end{aligned}\tag{69}$$

Note that a higher order expression of the stationary phase point and more complex NCS factors must be calculated when the residual phase in (65) has high dependency on the azimuth spatial variance. In this case, block processing in azimuth is more sensible to reduce the difficulty of processing.

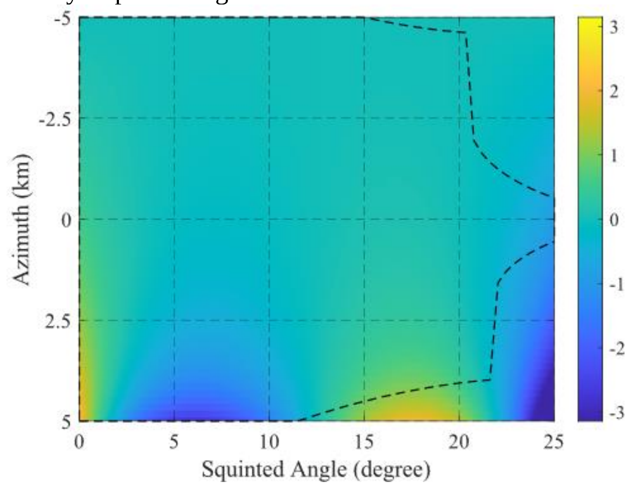

Fig. 7. The residual phase after azimuth processing.

The residual phase in (65) is analyzed by numerical experiment using the parameters in Table I. In Fig. 7, the x-axis represents the squinted angle, and the y-axis represents the azimuth coverage. The area within the black dashed line represents the area where the residual phase error is less than $\pi/4$. The residual phase increases as the squinted angle and the azimuth coverage increase. When the squinted angle is greater than 20°, the valid coverage shrinks rapidly. And it decreases to within 1km when the squinted angle reaches 25°. Therefore, block processing is necessary.

D. Geometric Correction

There also exists geometric distortion caused by the LRWC, which can be compensated by the geometric correction filter H_{13}.

$$H_{13}(f_\tau,t)=\exp\left(\frac{4\pi}{c}(f_\tau+f_c)\cdot v_{ref}\cdot\cos(\theta_c)\cdot t\right)\tag{70}$$

After Range IFFT, the focused SAR image is obtained as follows.

$$S_{13}(\tau,t;r,t_a)=\sin c\left(\tau-\frac{2r}{c}\right)\sin c\left(t-\alpha k_et_a\right)\exp\left(-j\frac{4\pi}{\lambda}r\right)\tag{71}$$

E. Computational Complexity Analysis

This section will analyze the computational complexity of the proposed algorithm and the referenced algorithm in [21]. Suppose N_a and N_r denote the azimuth and range pixel numbers. According to the flowchart in Fig. 3, the proposed algorithm includes three range FFTs/IFFTs, four azimuth FFTs/IFFTs, a range CZT, an azimuth convolution and eight phase multiplications. The range CZT is implemented by three FFTs with a length of $2N_r$, two phase multiplications with a length of N_r and a phase multiplication with a length of $2N_r$. The azimuth convolution is realized by two phase multiplications and an azimuth FFT. The computational load of the proposed algorithm is

$$\begin{aligned} O_1 &= 9N_aN_r\log_2 N_r + 5N_rN_a\log_2 N_a + 20N_aN_r \\ &= N_aN_r\left(9\log_2 N_r + 5\log_2 N_a + 20\right) \end{aligned} \quad (72)$$

Similarly, the computational load of the referenced algorithm in [21] is calculated as

$$\begin{aligned} O_2 &= 5N_aN_r\log_2 N_r + 4N_rN_a\log_2 N_a + 8N_aN_r \\ &= N_aN_r\left(5\log_2 N_r + 4\log_2 N_a + 8\right) \end{aligned} \quad (73)$$

It can be seen that the computational load of the proposed algorithm is greater than that of the referenced algorithm in [21]. The proposed algorithm is RMA-based, whereas the referenced algorithm in [21] is CS-based. The range CZT in the proposed algorithm significantly increases computational complexity but is more suitable for the focusing of high squint spaceborne SAR data.

IV. Experiments

A. Simulation Results

Experiments with simulated SAR data are carried out to verify the effectiveness of the proposed algorithm. The parameters are listed in Table I.

TABLE I
System Simulation Parameters

Parameters	Value
Orbit height(km)	600
Incidence Angle(°)	35.15
Squinted Angle(°)	20
Wavelength(m)	0.0311
Pulse width(s)	2e-6
PRF(Hz)	5000
Signal bandwidth(MHz)	300
Sampling rate(MHz)	450
Swath coverage(km^2)	5×5

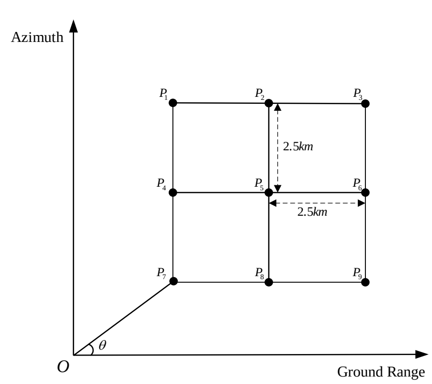

Fig. 8. Distribution of the simulated point targets.

Nine point targets are placed on the ground with regular intervals, and the scene size is $5km\times 5km$, as shown in Fig. 8. The layout of targets is consistent with [21]. The SAR system is operated in the sliding spotlight mode, and the squinted angle θ steadily changes with a certain steering rate and a center angle of 20°. The theoretical resolution of the range is about 0.45 m while the azimuth is about 0.5 m. Three targets marked by 1, 5, and 9 are selected for further comparison. Target 5 located at the center of the scene represents the best imaging results because its parameters are a perfect match with imaging parameters. Targets 1 and 9 located at the edge of the scene represent the worst imaging results because the difference between their parameters and imaging parameters is the maximum.

The referenced algorithm in [21] (abbreviated by MCS), the proposed algorithm with NCS method in [28] (abbreviated by RFD-NCS), and the proposed algorithm with INCS are used to process the simulated data for comparison. The key steps related to the focusing and de-aliasing performance of different methods are listed in Table II.

TABLE II
Performance Comparison of Different Methods

Method	Key steps	
	De-aliasing	Focusing
MCS	Range frequency-independent de-rotation	Third order azimuth frequency perturbation
RFD-NCS	Range frequency-dependent de-rotation	Fourth order azimuth frequency perturbation
Our method	Range frequency-dependent de-rotation	Improved NLCS algorithm based on the second-order approximations of the stationary phase point

Fig. 9 shows the interpolated contour plots of the point targets P_1, P_5, and P_9 obtained by the three algorithms. α is set to 0.98. Intuitively, the imaging results of the proposed algorithm with INCS are closest to the ideal one of a point target. The center target P_5 is well-focused by all three algorithms. For the edge targets P_1 and P_9, two-dimensional defocusing appears in the results of the referenced algorithm in [21] due to the high-order approximation of azimuth spectrum. Only azimuth defocusing exists in the results of the proposed algorithm with the NCS method in [28], which means the first-order approximation of the stationary phase point has significant errors. Only azimuth defocusing exists in the results of the proposed algorithm with the NCS method in [28], which means the first-order approximation of the stationary phase point has significant errors. As shown in Figs. 10 and 11, the range profiles and azimuth profiles also indicate that the proposed method with INCS is the most effective.

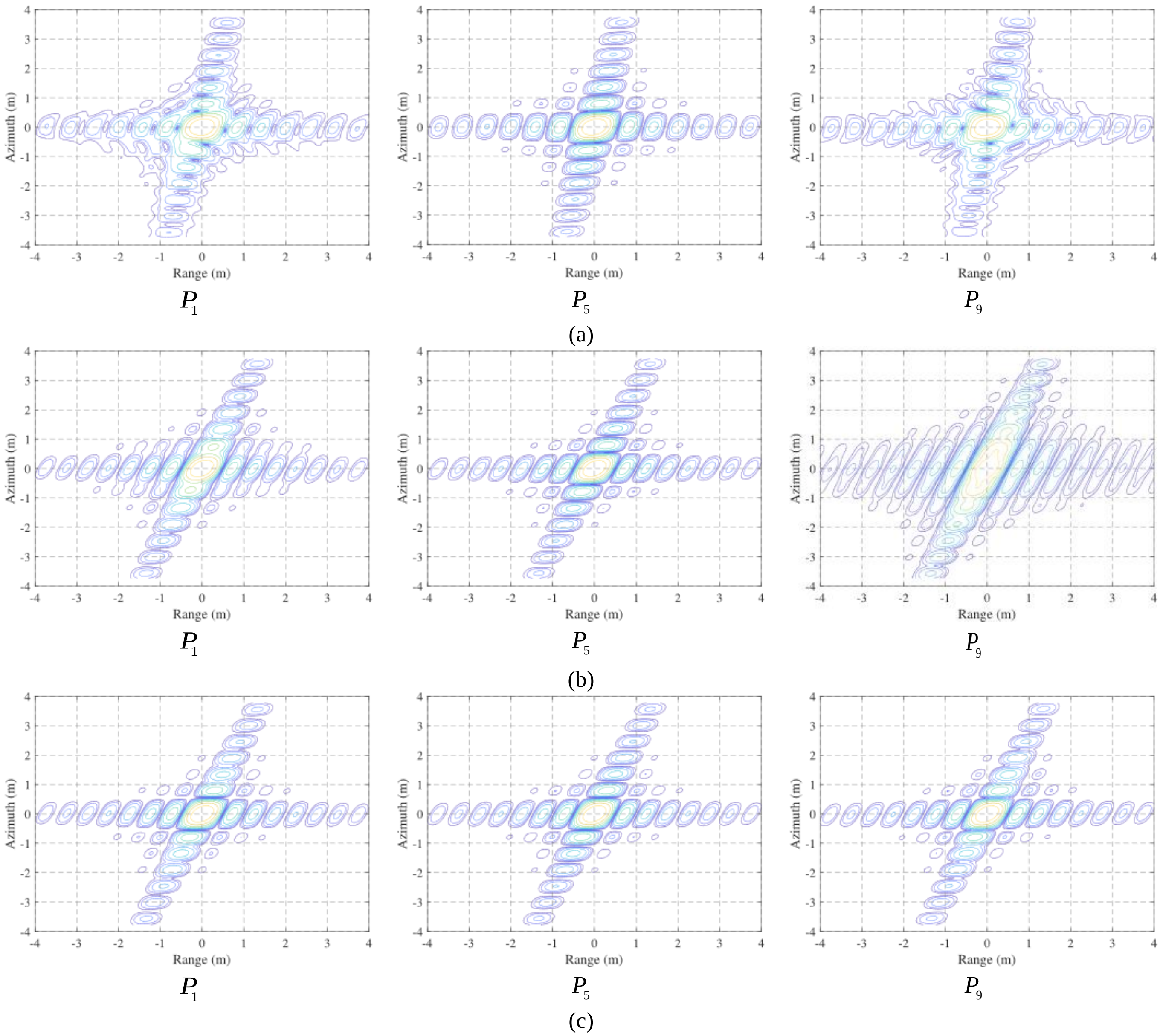

Fig. 9. Contour plots of three points obtained by different imaging algorithms, where the subfigure from left to right in each row correspond to targets 1, 5, and 9, respectively: (a) MCS algorithm (the referenced algorithm in [21]); (b) RFD-NCS (the proposed algorithm with NCS method in [28]); (c)proposed method.

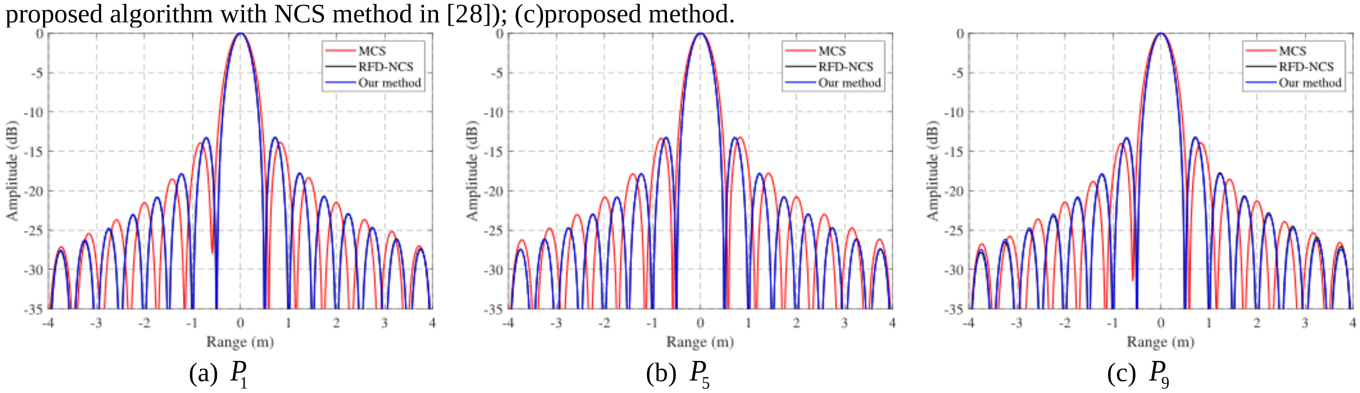

Fig. 10. Range profiles of three points obtained with different imaging algorithms: (a)-(c) is the result of the target P_1, P_5, and P_9, respectively.

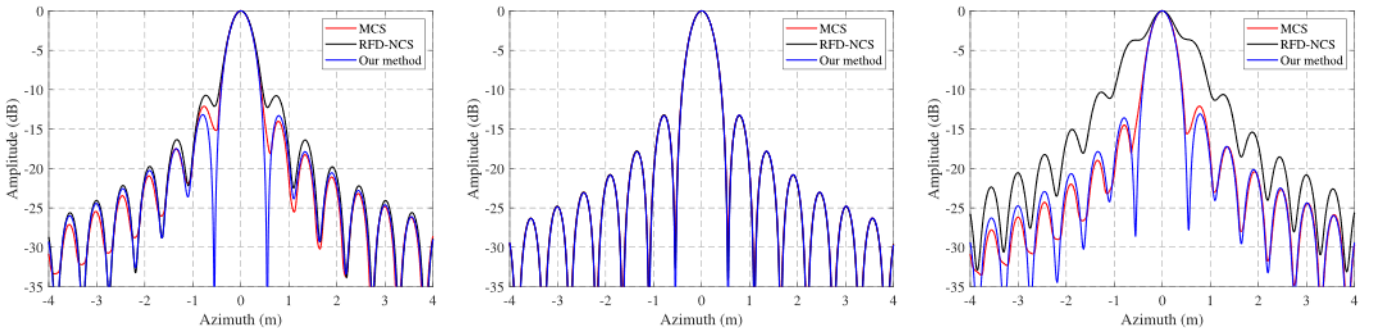

(a) P_1 (b) P_5 (c) P_9

Fig.11. Azimuth profiles of three points obtained with different imaging algorithms: (a)-(c) is the result of the target P_1, P_5, and P_9, respectively.

TABLE III
IMAGE QUALITY MEASUREMENT RESULTS

	Method	Azimuth			Range		
		Resolution(m)	PSLR(dB)	ISLR(dB)	Resolution(m)	PSLR(dB)	ISLR(dB)
P_1	MCS	0.4973	-12.095	-10.376	0.5157	-13.846	-11.433
	RFD-NCS	0.5122	-10.724	-8.500	0.4446	-13.250	-10.654
	Our method	0.4973	-13.164	-10.574	0.4446	-13.206	-10.629
P_5	MCS	0.4897	-13.259	-10.995	0.5092	-13.211	-10.773
	RFD-NCS	0.4955	-13.216	-10.971	0.4446	-13.262	-10.656
	Our method	0.4950	-13.231	-10.989	0.4446	-13.259	-10.656
P_9	MCS	0.5012	-12.084	-11.122	0.5207	-13.973	-11.640
	RFD-NCS	0.7164	-3.637	-7.331	0.4445	-12.593	-9.713
	Our method	0.4983	-13.102	-10.656	0.4446	-13.138	-10.623

To further evaluate the performance of the proposed algorithm, quantitative assessment results including resolution, peak sidelobe ratio (PSLR), and integrated sidelobe ratio (ISLR), are provided in Table III. It can be seen that the results of the proposed algorithm with INCS are the best in both range and azimuth. Furthermore, the comparison between the last two algorithms highlights the necessity of the second-order expression of the stationary phase point in NCS algorithms.

V. CONCLUSION

In this paper, a frequency-domain algorithm for squinted sliding-spotlight spaceborne SAR has been presented. It addresses the second-order coupling between the range frequency and Doppler parameters through range-frequency de-rotation and improved nonlinear chirp scaling. First, LRWC and the range frequency-dependent de-rotation operation are performed for thorough aliasing removal in the azimuth spectrum. Then, with a new signal model, focusing is completed by a modified RMA. Furthermore, a de-ramp operation with the improved NCS algorithm is derived to equalize the azimuth-variant phases based on the second-order expression of the stationary phase point. Finally, geometric correction is applied in the range-frequency domain. A well-focused image is obtained by the proposed algorithm, as demonstrated by the results based on simulated data.

The proposed algorithm does not involve approximation of the range spectrum which is necessary in traditional CS and RMA during the focusing process. Therefore, results in range are relatively better. Furthermore, focusing is achieved in the range frequency domain, indirectly avoiding the spatial variation of azimuth frequency modulation caused by LRWC. Defocusing of the azimuth signal is mainly caused by the differential RCM. After the range CZT, the negative effect of differential RCM is moved to the azimuth signal. It is solved by the improved NCS algorithm in our proposed solution.

In the future, the primary work is to test the proposed algorithm on real high-squint spaceborne SAR data to verify its applicability in practice. In addition, block processing can be combined with azimuth processing to reduce spatial variation of parameters and further improve the DOAF in azimuth.

APPENDIX

DERIVATION OF EQUATION (38)

According to (30), $H_f\left(f_t, v_r, \theta\right)$ varies with range r because of the spatial-variant properties of v_r and θ. Suppose

$$v_r \approx v_{ref} + k_{v_r} \cdot (r - r_{ref}) \tag{74}$$

$$\theta \approx \theta_c + k_\theta \cdot (r - r_{ref}) \tag{75}$$

where k_{v_r} and k_θ are the first-order coefficients, which can be calculated by numerical fitting. Expanding $H_f\left(f_t, v_r, \theta\right)$ into the first order Taylor series of $(r - r_{ref})$ yields

$$
\begin{aligned}
H_f\left(v_r,\theta\right) &= H_f(f_t,v_r,\theta)\Big|_{v_r=v_{ref},\theta=\theta_c} \\
&+\frac{\partial H_f\left(f_t,v_r,\theta\right)}{\partial v_r}\Bigg|_{v_r=v_{ref},\theta=\theta_c}\cdot(v_r-v_{ref}) \\
&+\frac{\partial H_f\left(f_t,v_r,\theta\right)}{\partial \theta}\Bigg|_{v_r=v_{ref},\theta=\theta_c}\cdot(\theta-\theta_c)+\Delta H_f \\
&\approx H_{f0}(f_t)+\frac{\partial H_f\left(f_t,v_r,\theta\right)}{\partial v_r}\Bigg|_{v_r=v_{ref},\theta=\theta}\cdot k_{v_r}\cdot(r-r_{ref}) \\
&+\frac{\partial H_f\left(f_t,v_r,\theta\right)}{\partial \theta}\Bigg|_{v_r=v_{ref},\theta=\theta_c}\cdot k_\theta\cdot(r-r_{ref})+\Delta H_f
\end{aligned} \tag{76}
$$

Let

$$H_{f0}(f_t)=H_f(f_t,v_r,\theta)\Big|_{v_r=v_{ref},\theta=\theta_c} \tag{77}$$

$$k_{v_r}^{'}=\frac{\partial H_f\left(v_r,\theta\right)}{\partial v_r}\Bigg|_{v_r=v_{ref},\theta=\theta_c}\cdot k_{v_r} \tag{78}$$

$$k_\theta^{'}=\frac{\partial H_f\left(v_r,\theta\right)}{\partial \theta}\Bigg|_{v_r=v_{ref},\theta=\theta_c}\cdot k_\theta \tag{79}$$

$r\cdot H_f\left(f_t,v_r,\theta\right)$ can be expressed as

$$
\begin{aligned}
r\cdot H_f\left(f_t,v_r,\theta\right) &= (r_{ref}+\Delta r)\cdot H_f\left(f_t,v_r,\theta\right) \\
&= r_{ref}\cdot H_{f0}(f_t)+H_f^{'}(f_t)\cdot\Delta r+\Delta H_f
\end{aligned} \tag{80}
$$

$$H_f^{'}(f_t)=H_{f0}(f_t)+r_{ref}\cdot k_{v_r}^{'}+r_{ref}\cdot k_\theta^{'} \tag{81}$$

References

[1] C. V. Jakowatz, D. Wahl, P. Eichel, D. C. Ghiglia, and P. A. Thompson, *Spotlight-Mode Synthetic Aperture Radar: A Signal Processing Approach.* Norwell, MA, USA: Kluwer, 1996.

[2] P. Prats, R. Scheiber, J. Mittermayer, A. Meta and A. Moreira, "Processing of Sliding Spotlight and TOPS SAR Data Using Baseband Azimuth Scaling," in *IEEE Transactions on Geoscience and Remote Sensing*, vol. 48, no. 2, pp. 770-780, Feb. 2010, doi: 10.1109/TGRS.2009.2027701.

[3] G. W. Davidson and I. Cumming, "Signal properties of spaceborne squint-mode SAR," in *IEEE Transactions on Geoscience and Remote Sensing*, vol. 35, no. 3, pp. 611-617, May 1997, doi: 10.1109/36.581976.

[4] ICEYE SAR Product Guide. https://www.iceye.com/hubfs/ Downloadables/ICEYE SAR Product Guide.pdf.

[5] V. Ignatenko, M. Nottingham, A. Radius, L. Lamentowski and D. Muff, "ICEYE Microsatellite SAR Constellation Status Update: Long Dwell Spotlight and Wide Swath Imaging Modes," 2021 IEEE International Geoscience and Remote Sensing Symposium IGARSS, Brussels, Belgium, 2021, pp. 1493-1496, doi: 10.1109/IGARSS47720.2021.9554486.

[6] Capella Space. Available online: https://www.capellaspace.com.

[7] D. Castelletti, G. Farquharson, C. Stringham, and D. Eddy, “Operational readiness of the Capella Space SAR System,” in IGARSS 2020-2020 IEEE International Geoscience and Remote Sensing Symposium. IEEE, 2020, pp. 3571–3573.

[8] Umbra. Available online: https://umbra.space.

[9] C. Wu, K. y. Liu and M. Jin, "Modeling and a Correlation Algorithm for Spaceborne SAR Signals," in *IEEE Transactions on Aerospace and Electronic Systems*, vol. AES-18, no. 5, pp. 563-575, Sept. 1982, doi: 10.1109/TAES.1982.309269.

[10] R. K. Raney, H. Runge, R. Bamler, I. G. Cumming and F. H. Wong, "Precision SAR processing using chirp scaling," in *IEEE Transactions on Geoscience and Remote Sensing*, vol. 32, no. 4, pp. 786-799, July 1994, doi: 10.1109/36.298008.

[11] C. Cafforio, C. Prati and F. Rocca, "SAR data focusing using seismic migration techniques," in *IEEE Transactions on Aerospace and Electronic Systems*, vol. 27, no. 2, pp. 194-207, March 1991, doi: 10.1109/7.78293.

[12] C. Prati, A. M. Guarnieri and F. Rocca, "Spot Mode Sar Focusing With The W - K Technique," *[Proceedings] IGARSS'91 Remote Sensing: Global Monitoring for Earth Management*, Espoo, Finland, 1991, pp. 631-634, doi: 10.1109/IGARSS.1991.579967.

[13] J. Mittermayer, A. Moreira and O. Loffeld, "Spotlight SAR data processing using the frequency scaling algorithm," in *IEEE Transactions on Geoscience and Remote Sensing*, vol. 37, no. 5, pp. 2198-2214, Sept. 1999, doi: 10.1109/36.789617.

[14] J. Mittermayer, R. Lord and E. Borner, "Sliding spotlight SAR processing for TerraSAR-X using a new formulation of the extended chirp scaling algorithm," IGARSS 2003. 2003 IEEE International Geoscience and Remote Sensing Symposium. Proceedings (IEEE Cat. No.03CH37477), Toulouse, France, 2003, pp. 1462-1464, doi: 10.1109/IGARSS.2003.1294144.

[15] R. Lanari, M. Tesauro, E. Sansosti and G. Fornaro, "Spotlight SAR data focusing based on a two-step processing approach," in *IEEE Transactions on Geoscience and Remote Sensing*, vol. 39, no. 9, pp. 1993-2004, Sept. 2001, doi: 10.1109/36.951090.

[16] R. Lanari, S. Zoffoli, E. Sansosti, G. Fornaro, F. Serafino, "New approach for hybrid strip-map/spotlight SAR data focusing," *IEE Proceedings-Radar, Sonar and Navigation*, 2001, 148, (6), pp. 363-372, doi: 10.1049/ip-rsn:20010662.

[17] W. Xu, Y. Deng, P. Huang and R. Wang, "Full-Aperture SAR Data Focusing in the Spaceborne Squinted Sliding-Spotlight Mode," in *IEEE Transactions on Geoscience and Remote Sensing*, vol. 52, no. 8, pp. 4596-4607, Aug. 2014, doi: 10.1109/TGRS.2013.2282863.

[18] W. Yang, J. Chen, W. Liu, P. Wang and C. Li, "A Modified Three-Step Algorithm for TOPS and Sliding Spotlight SAR Data Processing," in *IEEE Transactions on Geoscience and Remote Sensing*, vol. 55, no. 12, pp. 6910-6921, Dec. 2017, doi: 10.1109/TGRS.2017.2735993.

[19] W. Yang, J. Chen, H. Zeng, J. Zhou, P. Wang, C. Li, "A Novel Three-Step Image Formation Scheme for Unified Focusing on Spaceborne SAR Data," *Progress In*

Electromagnetics Research, Vol. 137, 621-642, 2013. doi:10.2528/PIER12122309.
[20] G. Engen and Y. Larsen, "Efficient Full Aperture Processing of TOPS Mode Data Using the Moving Band Chirp Z -Transform," in *IEEE Transactions on Geoscience and Remote Sensing*, vol. 49, no. 10, pp. 3688-3693, Oct. 2011, doi: 10.1109/TGRS.2011.2145384.
[21] J. Chen, H. Kuang, W. Yang, W. Liu and P. Wang, "A Novel Imaging Algorithm for Focusing High-Resolution Spaceborne SAR Data in Squinted Sliding-Spotlight Mode," in *IEEE Geoscience and Remote Sensing Letters*, vol. 13, no. 10, pp. 1577-1581, Oct. 2016, doi: 10.1109/LGRS.2016.2598066.
[22] D. Zhu et al., "An Extended Two Step Approach to High-Resolution Airborne and Spaceborne SAR Full-Aperture Processing," in *IEEE Transactions on Geoscience and Remote Sensing*, vol. 59, no. 10, pp. 8382-8397, Oct. 2021, doi: 10.1109/TGRS.2020.3033120.
[23] L. Sun, Z. Yu, C. Li, W. Liu, S. Wang and J. Geng, "An Imaging Algorithm for Spaceborne High-Squint L-Band SAR Based on Time-Domain Rotation," in *IEEE Journal of Selected Topics in Applied Earth Observations and Remote Sensing*, vol. 12, no. 12, pp. 5289-5299, Dec. 2019, doi: 10.1109/JSTARS.2019.2953836.
[24] F. H. Wong, Tat Soon Yeo and Ngee Leng Tan, "New applications of non-linear chirp scaling in SAR data processing," *IGARSS 2000. IEEE 2000 International Geoscience and Remote Sensing Symposium. Taking the Pulse of the Planet: The Role of Remote Sensing in Managing the Environment. Proceedings (Cat. No.00CH37120)*, Honolulu, HI, USA, 2000, pp. 96-98 vol.1, doi: 10.1109/IGARSS.2000.860433.
[25] D. An, X. Huang, T. Jin and Z. Zhou, "Extended Nonlinear Chirp Scaling Algorithm for High-Resolution Highly Squint SAR Data Focusing," in *IEEE Transactions on Geoscience and Remote Sensing*, vol. 50, no. 9, pp. 3595-3609, Sept. 2012, doi: 10.1109/TGRS.2012.2183606.
[26] G. Sun, X. Jiang, M. Xing, Z. -j. Qiao, Y. Wu and Z. Bao, "Focus Improvement of Highly Squinted Data Based on Azimuth Nonlinear Scaling," in *IEEE Transactions on Geoscience and Remote Sensing*, vol. 49, no. 6, pp. 2308-2322, June 2011, doi: 10.1109/TGRS.2010.2102040.
[27] M. Xing, Y. Wu, Y. D. Zhang, G. -C. Sun and Z. Bao, "Azimuth Resampling Processing for Highly Squinted Synthetic Aperture Radar Imaging With Several Modes," in *IEEE Transactions on Geoscience and Remote Sensing*, vol. 52, no. 7, pp. 4339-4352, July 2014, doi: 10.1109/TGRS.2013.2281454.
[28] X. Qiu, D. Hu and C. Ding, "An Improved NLCS Algorithm With Capability Analysis for One-Stationary BiSAR," in *IEEE Transactions on Geoscience and Remote Sensing*, vol. 46, no. 10, pp. 3179-3186, Oct. 2008, doi: 10.1109/TGRS.2008.921569.
[29] Z. Li, Y. Liang, M. Xing, Y. Huai, L. Zeng and Z. Bao, "Focusing of Highly Squinted SAR Data With Frequency Nonlinear Chirp Scaling," in *IEEE Geoscience and Remote Sensing Letters*, vol. 13, no. 1, pp. 23-27, Jan. 2016, doi: 10.1109/LGRS.2015.2492681.
[30] H. Zhong, S. Zhang, J. Hu and M. Sun, "Focusing Nonparallel-Track Bistatic SAR Data Using Extended Nonlinear Chirp Scaling Algorithm Based on a Quadratic Ellipse Model," in *IEEE Geoscience and Remote Sensing Letters*, vol. 14, no. 12, pp. 2390-2394, Dec. 2017, doi: 10.1109/LGRS.2017.2765741.
[31] G. -C. Sun, Y. Wu, J. Yang, M. Xing and Z. Bao, "Full-Aperture Focusing of Very High Resolution Spaceborne-Squinted Sliding Spotlight SAR Data," in *IEEE Transactions on Geoscience and Remote Sensing*, vol. 55, no. 6, pp. 3309-3321, June 2017, doi: 10.1109/TGRS.2017.2669205.
[32] Y. L. Neo, F. Wong and I. G. Cumming, "A Two-Dimensional Spectrum for Bistatic SAR Processing Using Series Reversion," in *IEEE Geoscience and Remote Sensing Letters*, vol. 4, no. 1, pp. 93-96, Jan. 2007, doi: 10.1109/LGRS.2006.885862.
[33] B. Liu, T. Wang, Q. Wu and Z. Bao, "Bistatic SAR Data Focusing Using an Omega-K Algorithm Based on Method of Series Reversion," in *IEEE Transactions on Geoscience and Remote Sensing*, vol. 47, no. 8, pp. 2899-2912, Aug. 2009, doi: 10.1109/TGRS.2009.2017522.
[34] I. G. Cumming, and F. H. Wong. *"Digital Signal Processing of Synthetic Aperture Radar Data: Algorithms and Implementation: Artech House."* (2005).
[35] B. Bie, G. -C. Sun, X. -G. Xia, M. Xing, L. Guo and Z. Bao, "High-Speed Maneuvering Platforms Squint Beam-Steering SAR Imaging Without Subaperture," in *IEEE Transactions on Geoscience and Remote Sensing*, vol. 57, no. 9, pp. 6974-6985, Sept. 2019, doi: 10.1109/TGRS.2019.2909729.
[36] L. Rabiner, R. Schafer and C. Rader, "The chirp z-transform algorithm," in *IEEE Transactions on Audio and Electroacoustics*, vol. 17, no. 2, pp. 86-92, June 1969, doi: 10.1109/TAU.1969.1162034.